On Merging High- and Low-Resolution DEMs From TOPSAR and SRTM Using a Prediction-Error Filter

Sang-Ho Yun, *Student Member, IEEE*, Jun Ji, Howard Zebker, *Fellow, IEEE*, and Paul Segall

Abstract—High-resolution digital elevation models (DEMs) are often limited in spatial coverage; they also may possess systematic artifacts when compared to comprehensive low-resolution maps. Here we correct artifacts and interpolate regions of missing data in airborne Topographic Synthetic Aperture Radar (TOPSAR) DEMs using a low-resolution Shuttle Radar Topography Mission (SRTM) DEM. We use a prediction error (PE) filter to interpolate and fill missing data so that the interpolated regions have the same spectral content as the valid regions of the TOPSAR DEM. The SRTM DEM is used as an additional constraint in the interpolation. We use cross-validation methods to obtain the optimal weighting for the PE filter and SRTM DEM constraints.

Index Terms—Interpolation, digital elevation model (DEM), Topographic Synthetic Aperture Radar (TOPSAR), Shuttle Radar Topography Mission (SRTM), inversion, prediction error (PE) filter.

I. INTRODUCTION

SYNTHETIC aperture radar interferometry (InSAR) is a powerful tool for generating digital elevation models (DEMs) [1]. The TOPSAR and SRTM sensors are primary sources for the academic community for DEMs derived from single-pass interferometric data. Differences in system parameters such as altitude and swath width (Table I) result in very different properties for derived DEMs. Specifically, TOPSAR DEMs have better resolution, while SRTM DEMs have better accuracy over larger areas. TOPSAR coverage is often not spatially complete.

Topographic Synthetic Aperture Radar (TOPSAR) DEMs are produced from cross-track interferometric data acquired with the National Aeronautics and Space Administration's Airborne Synthetic Aperture Radar (AIRSAR) system mounted on a DC-8 aircraft. Although the TOPSAR DEMs have a higher resolution than other existing data, they sometimes suffer from artifacts and missing data due to roll of the aircraft, layover, and flight planning limitations. The DEMs derived from the Shuttle Radar Topography Mission (SRTM) have lower resolution, but fewer artifacts and missing data than TOPSAR DEMs. Thus, the former often provides information in the missing regions of the latter.

We illustrate joint use of these datasets using DEMs acquired over the Galápagos Islands. Fig. 1 shows the TOPSAR DEM

TABLE I
TOPSAR MISSION VERSUS SRTM MISSION

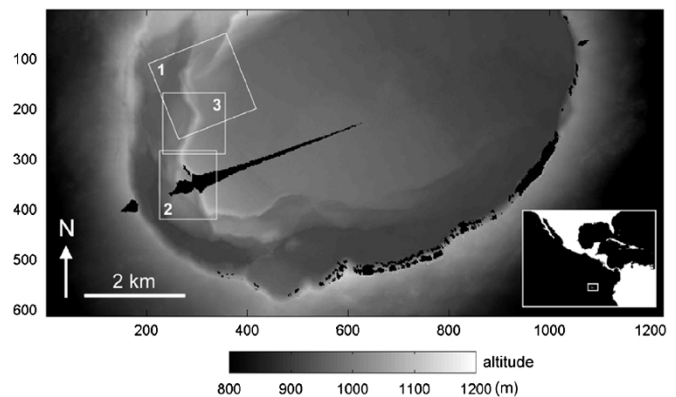| Mission	TOPSAR	SRTM
Platform	DC-8 aircraft	Space shuttle
Nominal altitude	9 km	233 km
Swath width	10 km	225 km
Baseline	2.583 m	60 m
DEM resolution	10 m	90 m
DEM coord. system	none	Lat/Lon

Fig. 1. Original TOPSAR DEM of Sierra Negra volcano in the Galápagos Islands (inset for location). The pixel spacing of the image is 10 m. The boxed areas are used for illustration later in this paper. Note that there are a number of regions of missing data with various shapes and sizes. Artifacts are not identifiable due to the variation in topography.

used in this study. The DEM covers Sierra Negra volcano on the island of Isabela. Recent InSAR observations reveal that the volcano has been deforming relatively rapidly [2], [3]. InSAR analysis can require use of a DEM to produce a simulated interferogram required to isolate ground deformation. The effect of artifact elimination and interpolation for deformation studies will be discussed later in this paper.

The TOPSAR DEMs have a pixel spacing of about 10 m, sufficient for most geodetic applications. However, regions of missing data are often encountered (Fig. 1), and significant residual artifacts are found (Fig. 2). The regions of missing data are caused by layover of the steep volcanoes and by flight planning limitations. Artifacts are large-scale and systematic and most likely due to uncompensated roll of the DC-8 aircraft [4]. Attempts to compensate this motion include models of piecewise linear imaging geometry [5] and estimating imaging parameters that minimize the difference between the TOPSAR DEM and an independent reference DEM [6]. We use a nonparameterized direct approach by subtracting the difference between the TOPSAR and SRTM DEMs.

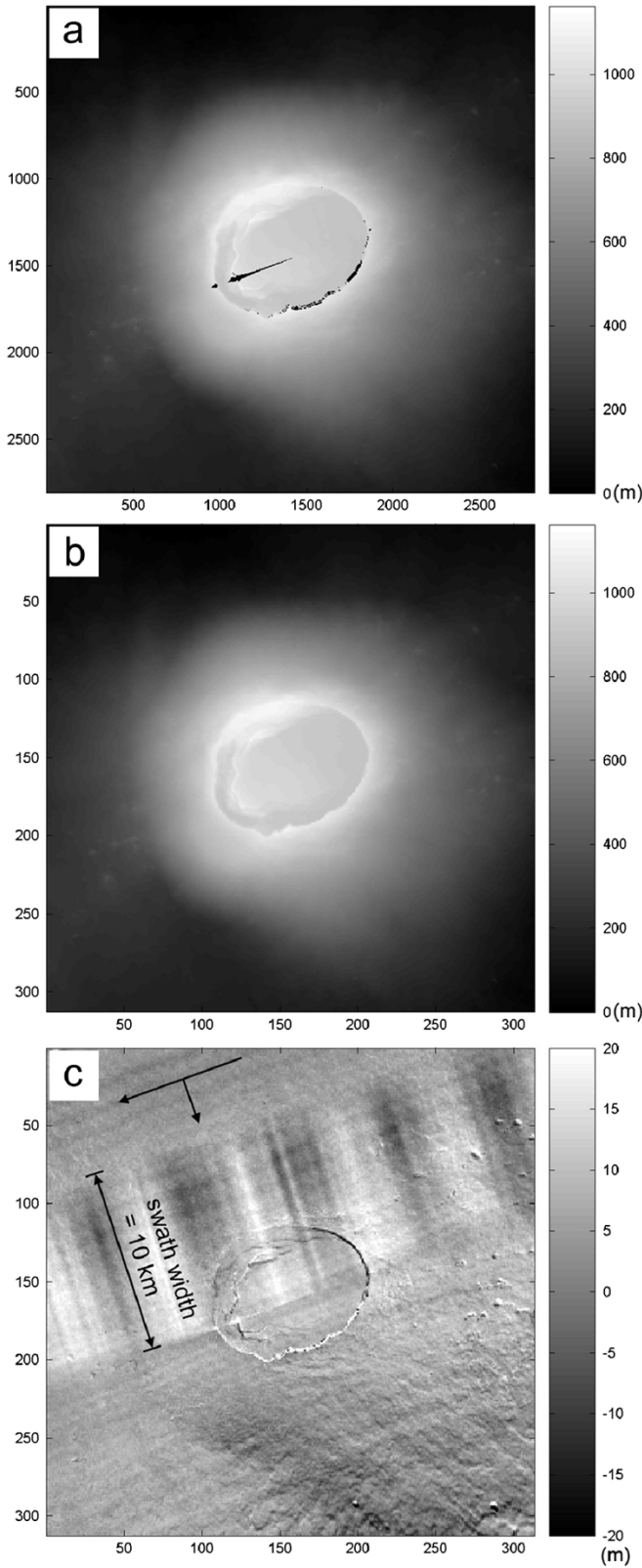Fig. 3. The flow-diagram of the artifact elimination.

Fig. 2. (a) TOPSAR DEM and (b) SRTM DEM. The tick labels are pixel numbers. Note the difference in pixel spacing between the two DEMs. (c) Artifacts obtained by subtracting the SRTM DEM from the TOPSAR DEM. The flight direction and the radar look direction of the aircraft associated with the swath with the artifact are indicated with a long and short arrows, respectively. Note that the artifacts appear in one entire TOPSAR swath, while it is not as serious in other swaths.

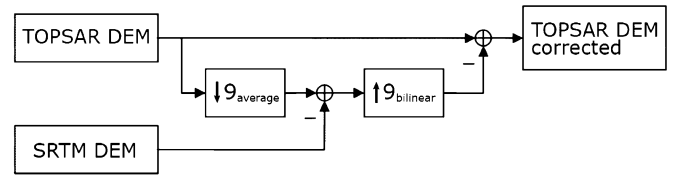The recent SRTM mission produced nearly worldwide topographic data at 90-m posting. SRTM topographic data are in fact produced at 30-m posting (1 arcsecond); however, high-resolution datasets for areas outside of the U.S. are not available to the public at this time. Only DEMs at 90-m posting (3 arcsecond) are available to download. For many analyses, finer scale elevation data are required. For example, a typical pixel spacing in a spaceborne SAR image is 20 m. If the SRTM DEMs are used for topography removal in spaceborne interferometry, the pixel spacing of the final interferograms would be limited by the topography data to at best 90 m. Despite the lower resolution, the SRTM DEM is useful because it has fewer motion-induced artifacts than the TOPSAR DEM. It also has fewer data holes.

The merits and demerits of the two DEMs are in many ways complementary to each other. Thus, a proper data fusion method can overcome the shortcomings of each and produce a new DEM that combines the strengths of the two datasets: a DEM that has a resolution of the TOPSAR DEM and large-scale reliability of the SRTM DEM. In this paper, we present an interpolation method that uses both TOPSAR and SRTM DEMs as constraints.

II. IMAGE REGISTRATION

The original TOPSAR DEM, while in ground-range coordinates, is not georeferenced. Thus, we register the TOPSAR DEM to the SRTM DEM, which is already registered in a latitude/longitude coordinate system. The image registration is carried out between the DEM datasets using an affine transformation. Although the TOPSAR DEM is not georeferenced, it is already on the ground coordinate system. Thus, scaling and rotation are the two most important components. We have seen that skewing component was negligible. Any higher order transformation between the two DEMs would also be negligible. The affine transformation used is as follows:

$$\begin{bmatrix} x_S \\ y_S \end{bmatrix} = \begin{bmatrix} a & b \\ c & d \end{bmatrix} \begin{bmatrix} x_T \\ y_T \end{bmatrix} + \begin{bmatrix} e \\ f \end{bmatrix} \tag{1}$$

where $\begin{bmatrix} x_S \\ y_S \end{bmatrix}$ and $\begin{bmatrix} x_T \\ y_T \end{bmatrix}$ are tie points in the SRTM and TOPSAR DEM coordinate systems respectively. Since $[a\ b\ e]$ and $[c\ d\ f]$ are estimated separately, at least three tie points are required to uniquely determine them. We picked ten tie points from each DEM based on topographic features and solved for the six unknowns in a least squares sense.

Given the six unknowns, we choose new georeferenced sample locations that are uniformly spaced; every ninth sample location corresponds to the sample location of SRTM DEM. Those sample locations form $\begin{bmatrix} x_S \\ y_S \end{bmatrix}$, and $\begin{bmatrix} x_T \\ y_T \end{bmatrix}$ is calculated. Then, the nearest TOPSAR DEM value is selected and is put into the corresponding new georeferenced sample location.
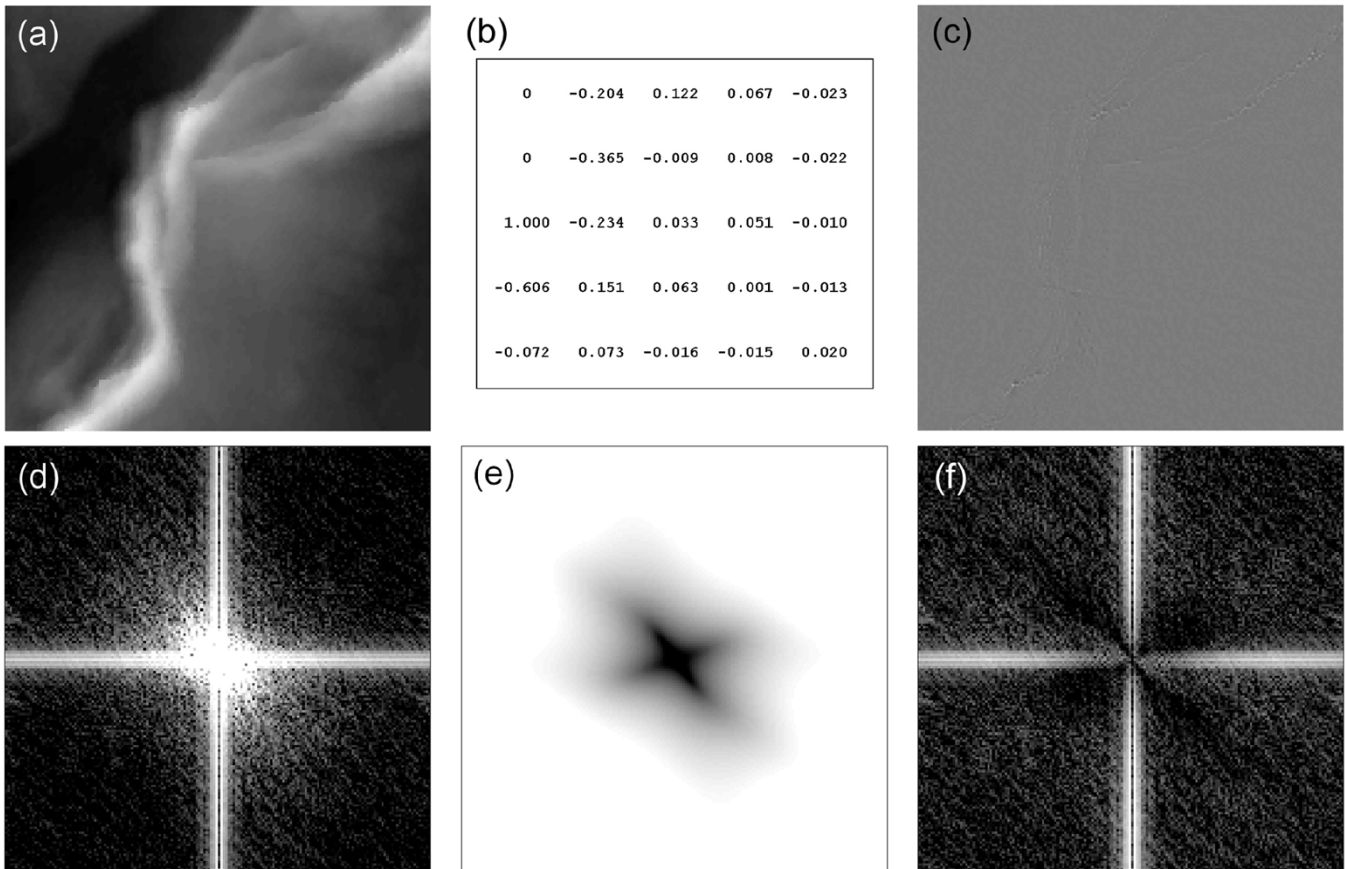
Fig. 4. Effect of a PE filter. (a) Original DEM. (b) A 2-D PE filter found from the DEM. (c) DEM filtered with the PE filter. (d)–(f) Spectra of (a)–(c), respectively, plotted in decibels. (a) and (c) are drawn with the same color scale. Note that in (c) the variation of image (a) was effectively suppressed by the filter. The standard deviations of (a) and (c) are 27.6 and 2.5 m, respectively.

The intermediate values are filled in from the TOPSAR map to produce the georeferenced 10-m dataset.

It should be noted that it is not easy to determine the tie points in DEM datasets. Enhancing the contrast of the DEMs facilitated the process. In general, fine registration is important for correctly merging different datasets. The two DEMs in this study have different pixel spacings. It is difficult to pick tie points with higher precision than the pixel spacing of the coarser image. In our method, however, the SRTM DEM, the coarser image, is treated as an averaged image of the TOPSAR DEM, the finer image. In our inversion, only the 9×9 averaged values of the TOPSAR DEM are compared with the pixel values of the SRTM DEM. Thus, the fine registration is less critical in this approach than in the case where one-to-one match is required.

III. ARTIFACT ELIMINATION

Examination of the georeferenced TOPSAR DEM [Fig. 2(a)] shows motion artifacts when compared to the SRTM DEM [Fig. 2(b)]. The artifacts are not clearly discernible in Fig. 2(a) because their magnitude is small in comparison to the overall data values. The artifacts are identified by downsampling the registered TOPSAR DEM and subtracting the SRTM DEM. Large-scale anomalies that periodically fluctuate over an entire swath are visible in Fig. 2(c). The periodic pattern is most likely

due to uncompensated roll of the DC-8 aircraft. The spaceborne data are less likely to exhibit similar artifacts, because the spacecraft is not greatly affected by the atmosphere. Note that the width of the anomalies corresponds to the width of a TOPSAR swath. Because the SRTM swath is much larger than that of the TOPSAR system (Table I), a larger area is covered under consistent conditions, reducing the number of parallel tracks required to form an SRTM DEM.

The maximum amplitude of the motion artifacts in our study area is about 20 m. This would result in substantial errors in many analyses if not properly corrected. For example, if this TOPSAR DEM is used for topography reduction in repeat-pass InSAR using ERS-2 data with a perpendicular baseline of about 400 m, the resulting deformation interferogram would contain one fringe ($= 2.8$ cm) of spurious signal.

To remove these artifacts from the TOPSAR DEM, we upsample the difference image with bilinear interpolation by a factor of nine so that its pixel spacing matches the TOPSAR DEM. The difference image is subtracted from the TOPSAR DEM. This process is described with a flow-diagram in Fig. 3. Note that the lower branch undergoes two low-pass filter operations when averaging and bilinear interpolation are implemented, while the upper branch preserves the high-frequency contents of the TOPSAR DEM. In this way we can eliminate the large-scale artifacts while retaining details in the TOPSAR DEM.

IV. PREDICTION ERROR FILTER

The next step in the DEM process is to fill in missing data. We use a prediction error (PE) filter operating on the TOPSAR DEM to fill these gaps. The basic idea of the PE filter constraint [7], [8] is that missing data can be estimated so that the restored data yield minimum energy when the PE filter is applied. The PE filter is derived from training data, which is normally valid data surrounding the missing region. The PE filter is selected so that the missing data and the valid data share the same spectral content.

Hence, we assume that the spectral content of the missing data in the TOPSAR DEM is similar to that of the regions with valid data surrounding the missing regions. We generate a PE filter such that it rejects data with statistics found in the valid regions of the TOPSAR DEM. Given this PE filter, we solve for data in the missing regions such that the interpolated data is also been nullified by the PE filter. This concept is illustrated in Fig. 5.

The PE filter $\mathbf{f}_{\mathrm{PE}}$ is found by minimizing the following objective function:

$$\|\mathbf{f}_{\mathrm{PE}} * \mathbf{x}_e\|^2 \tag{2}$$

where $\mathbf{x}_e$ is the existing data from the TOPSAR DEM, and $*$ represents convolution. This expression can be rewritten in a linear algebraic form using the following matrix operation:

$$\|\mathbf{F}_{\mathrm{PE}}\mathbf{x}_e\|^2 \tag{3}$$

or equivalently

$$\|\mathbf{X}_e\mathbf{f}_{\mathrm{PE}}\|^2 \tag{4}$$

where $\mathbf{F}_{\mathrm{PE}}$ and $\mathbf{X}_e$ are the matrix representations of $\mathbf{f}_{\mathrm{PE}}$ and $\mathbf{x}_e$ for the convolution operation. These matrix and vector expressions are used to indicate their linear relationship.

The procedure of acquiring the PE filter can be explained with one-dimensional example. Suppose that a dataset $\mathbf{x} = [x_1, \ldots, x_n]$ (where $n \gg 3$) is given, and we want to compute a PE filter of length 3, $\mathbf{f}_{\mathrm{PE}} = [1\ f_1\ f_2]$. Then we form a system of linear equations as follows:

$$\begin{bmatrix} x_3 & x_2 & x_1 \\ x_4 & x_3 & x_2 \\ \vdots & \vdots & \vdots \\ x_n & x_{n-1} & x_{n-2} \end{bmatrix} \begin{bmatrix} 1 \\ f_1 \\ f_2 \end{bmatrix} \approx 0. \tag{5}$$

The first element of the PE filter should be equal to one to avoid the trivial solution, $\mathbf{f}_{\mathrm{PE}} = \mathbf{0}$. Note that (5) is the convolution of the data and the PE filter. After simple algebra and with

$$\mathbf{d} \equiv \begin{bmatrix} x_3 \\ \vdots \\ x_n \end{bmatrix} \quad \mathbf{D} \equiv \begin{bmatrix} x_2 & x_1 \\ \vdots & \vdots \\ x_{n-1} & x_{n-2} \end{bmatrix}$$

we get

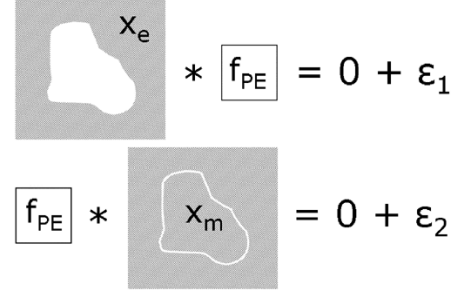$$\mathbf{D} \begin{bmatrix} f_1 \\ f_2 \end{bmatrix} \approx -\mathbf{d} \tag{6}$$

Fig. 5. Concept of PE filter. The PE filter is estimated by solving an inverse problem constrained with the remaining part, and the missing part is estimated by solving another inverse problem constrained with the filter. The ε_1 and ε_2 are white noise with small amplitude.

and its normal equation becomes

$$\begin{bmatrix} f_1 \\ f_2 \end{bmatrix} = (\mathbf{D}^T\mathbf{D})^{-1}\mathbf{D}^T(-\mathbf{d}). \tag{7}$$

Note that (7) minimizes (2) in a least squares sense. This procedure can be extended to two-dimensional (2-D) problems, and more details are described in [7] and [8].

Fig. 4 shows the characteristics of the PE filter in the spatial and Fourier domains. Fig. 4(a) is the sample DEM chosen from Fig. 1 (numbered box 1) for demonstration. It contains various topographic features, and has a wide range of spectral content [Fig. 4(d)]. Fig. 4(b) is the 5×5 PE filter derived from 4(a) by solving the inverse problem in (3). Note that the first three elements in the first column of the filter coefficients are 0 0 1. This is the PE filter's unique constraint that ensures the filtered output to be white noise [7]. In the filtered output [Fig. 4(c)] all the variations in the DEM were effectively suppressed. The size (order) of the PE filter is based on the complexity of the spectrum of the DEM. In general, as the spectrum becomes more complex, a larger size filter is required. After testing various sizes of the filter, we found a 5×5 size appropriate for the DEM used in our study. Fig. 4(d) and (e) shows the spectra of the DEM and the PE filter respectively. These illustrate the inverse relationship of the PE filter to the corresponding DEM in the Fourier domain, such that their product is minimized [Fig. 4(f)]. This PE filter constrains the interpolated data in the DEM to similar spectral content to the existing data.

All inverse problems in this study were derived using the conjugate gradient method, where forward and adjoint functional operators are used instead of the explicit inverse operators [7], saving computer memory space.

V. INTERPOLATION

Once the PE filter is determined, we next estimate the missing parts of the image. As depicted in Fig. 5, interpolation using the PE filter requires that the norm of the filtered output be minimized. This procedure can be formulated as an inverse computation minimizing the following objective function:

$$\|\mathbf{F}_{\mathrm{PE}}\mathbf{x}\|^2 \tag{8}$$

where $\mathbf{F}_{\mathrm{PE}}$ is the matrix representation of the PE filter convolution, and $\mathbf{x}$ represents the entire dataset including the known
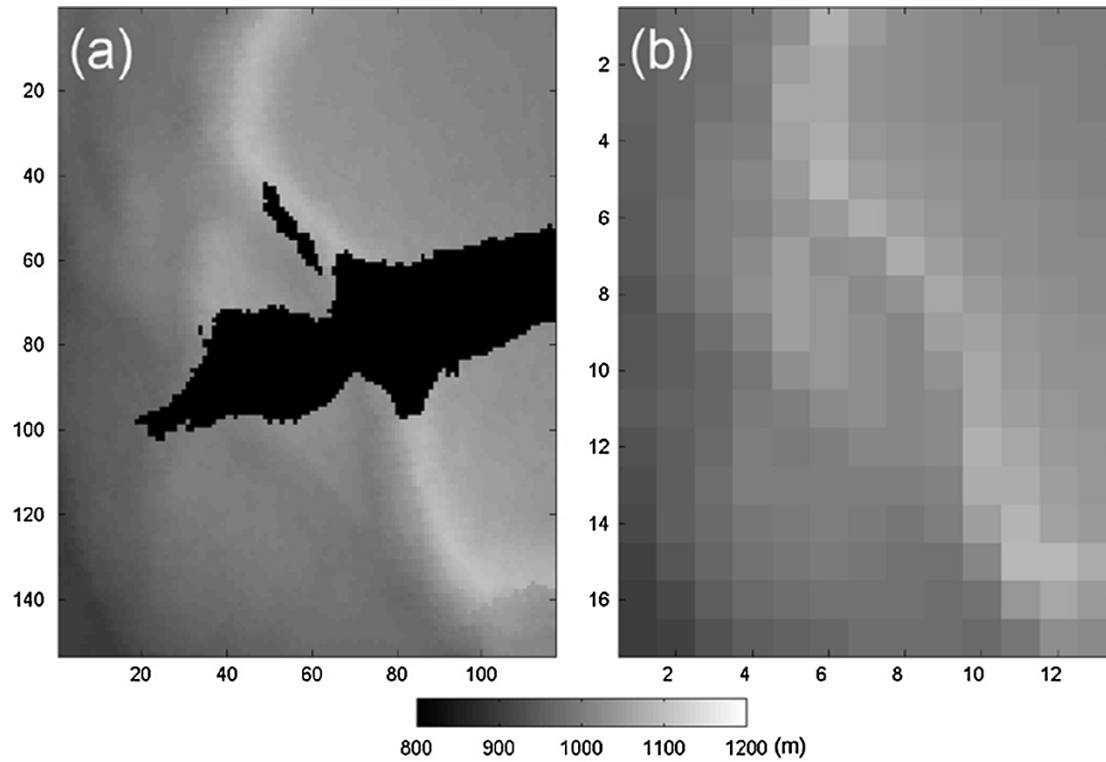
Fig. 6. Example subimages of (a) TOPSAR DEM showing regions of missing data (black) and (b) SRTM DEM of the same area. These subimages are engaged in one implementation of the interpolation. The grayscale is altitude in meters.

and the missing regions. In the inversion process we only update the missing region, without changing the known region. This guarantees seamless interpolation across the boundaries between the known and missing regions. As previously stated, 90-m posting SRTM DEMs were generated from 30-m posting data. This downsampling was done by calculating three "looks" in both the easting and northing directions. In order to use the SRTM DEM as a constraint to interpolate the TOPSAR DEM, we posit the following relationship between the two DEMs: each pixel value in a 90-m posting SRTM DEM can be considered equivalent to the averaged value of a 9×9 pixel window in a 10-m posting TOPSAR DEM centered at the corresponding pixel in the SRTM DEM.

Solution using the constraint of the SRTM DEM to find the missing data points in the TOPSAR DEM can be expressed as minimizing the following objective function:

$$\|\mathbf{y} - \mathbf{A}\mathbf{x}_m\|^2 \tag{9}$$

where $\mathbf{y}$ is an SRTM DEM expressed as a vector that covers the missing regions of the TOPSAR DEM, and $\mathbf{A}$ is an averaging operator generating nine looks, and $\mathbf{x}_m$ represents the missing regions of the TOPSAR DEM.

By combining two constraints, one derived from the statistics of the PE filter and one from the SRTM DEM, we can interpolate the missing data optimally with respect to both criteria. The PE filter guarantees that the interpolated data will have the same spectral properties as the known data. At the same time the SRTM constraint forces the interpolated data to have average height near the corresponding SRTM DEM. We formulate the
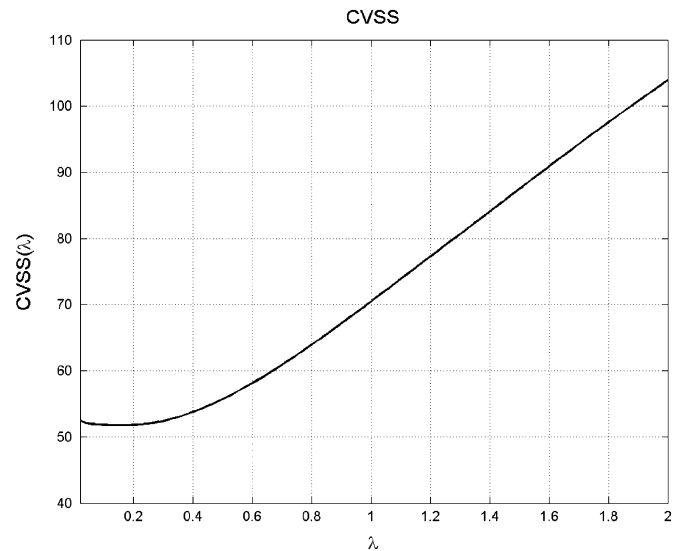

Fig. 7. Cross-validation sum of squares. The minimum occurs when $\lambda = 0.16$.

inverse problem as a minimization of the following objective function:

$$\lambda^2\|\mathbf{F}_{\mathrm{PE}}\mathbf{x}_m\|^2 + \|\mathbf{y} - \mathbf{A}\mathbf{x}_m\|^2 \tag{10}$$

where λ set the relative effect of each criterion. Here $\mathbf{x}_m$ has the dimensions of the TOPSAR DEM, while $\mathbf{y}$ has the dimensions of the SRTM DEM. If regions of missing data are localized in an image, entire image does not have to be used for generating a PE filter. We implement interpolation in subimages to save time and computer memory space. An example of the such subimage is
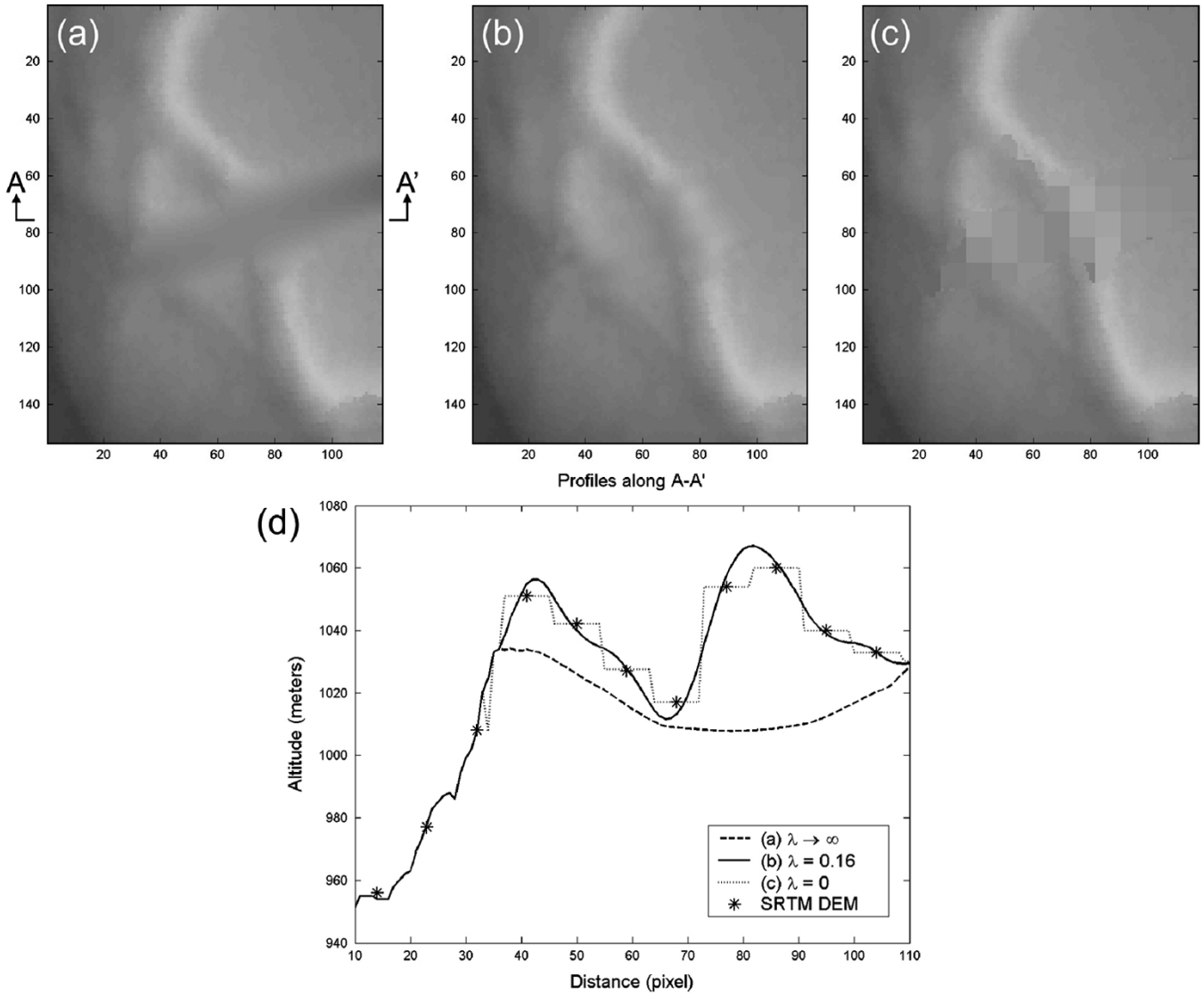
Fig. 8.   Results of interpolation applied to DEMs in Fig. 6, with various weights. (a) $\lambda \to \infty$. (b) $\lambda = 0.16$. (c) $\lambda = 0$. Profiles along $A - A'$ are shown in (d).

shown in Fig. 6. The image is a part of Fig. 1 (numbered box 2). Fig. 6(a) and (b) shows examples of $\mathbf{x}_e$ in (3) and $\mathbf{y}$, respectively.

The multiplier λ determines the relative weight of the two terms in the objective function. As $\lambda \to \infty$, the solution satisfies the first constraint only, and if $\lambda = 0$, the solution satisfies the second constraint only.

We used cross-validation sum of squares (CVSS) [9] to determine the optimal weights for the two terms in (10). Consider a model $\mathbf{x}_m$ that minimizes the following quantity:

$$\lambda^2 \|\mathbf{F}_{\mathrm{PE}}\mathbf{x}_m\|^2 + \|\mathbf{y}^{(k)} - \mathbf{A}^{(k)}\mathbf{x}_m\|^2 \qquad (k = 1, \ldots, N) \quad (11)$$

where $\mathbf{y}^{(k)}$ and $\mathbf{A}^{(k)}$ are the $\mathbf{y}$ and the $\mathbf{A}$ in (10) with the kth element and the kth row omitted respectively, and N is the number of elements in $\mathbf{y}$ that fall into the missing region. Denote this model $\mathbf{x}_m^{(k)}(\lambda)$. Then we compute the CVSS defined as follows:

$$\mathrm{CVSS}(\lambda) = \frac{1}{N} \sum_{k=1}^{N} \left(y_k - A_k \mathbf{x}_m^{(k)}(\lambda) \right)^2 \qquad (12)$$

where y_k is the omitted element from the vector $\mathbf{y}$ and A_k is the omitted row vector from the matrix $\mathbf{A}$ when the $\mathbf{x}_m^{(k)}(\lambda)$ was estimated. Thus, $A_k\mathbf{x}_m^{(k)}(\lambda)$ is the prediction based on the other $N-1$ observations. Finally, we minimize $\mathrm{CVSS}(\lambda)$ with respect to λ to obtain the optimal weight (Fig. 7).

In the case of the example shown in Fig. 6, the minimum CVSS was obtained for $\lambda = 0.16$ (Fig. 7). The effect of varying λ is shown in Fig. 8. It is apparent (see Fig. 8) that the optimal weight is a more "plausible" result than either of the end members, preserving aspects of both constraints.

In Fig. 8(a) the interpolation uses only the PE filter constraint. This interpolation does not recover the continuity of the ridge running across the DEM in north–south direction, which is observed in the SRTM DEM [Fig. 6(b)]. This follows from a PE filter obtained such that it eliminates the overall variations in the image. The variations include not only the ridge but also the accurate topography in the DEM.

The other end member, Fig. 8(c), shows the result for applying zero weight to the PE filter constraint. Since the averaging operator $\mathbf{A}$ in (10) is applied independently for each 9×9 pixel
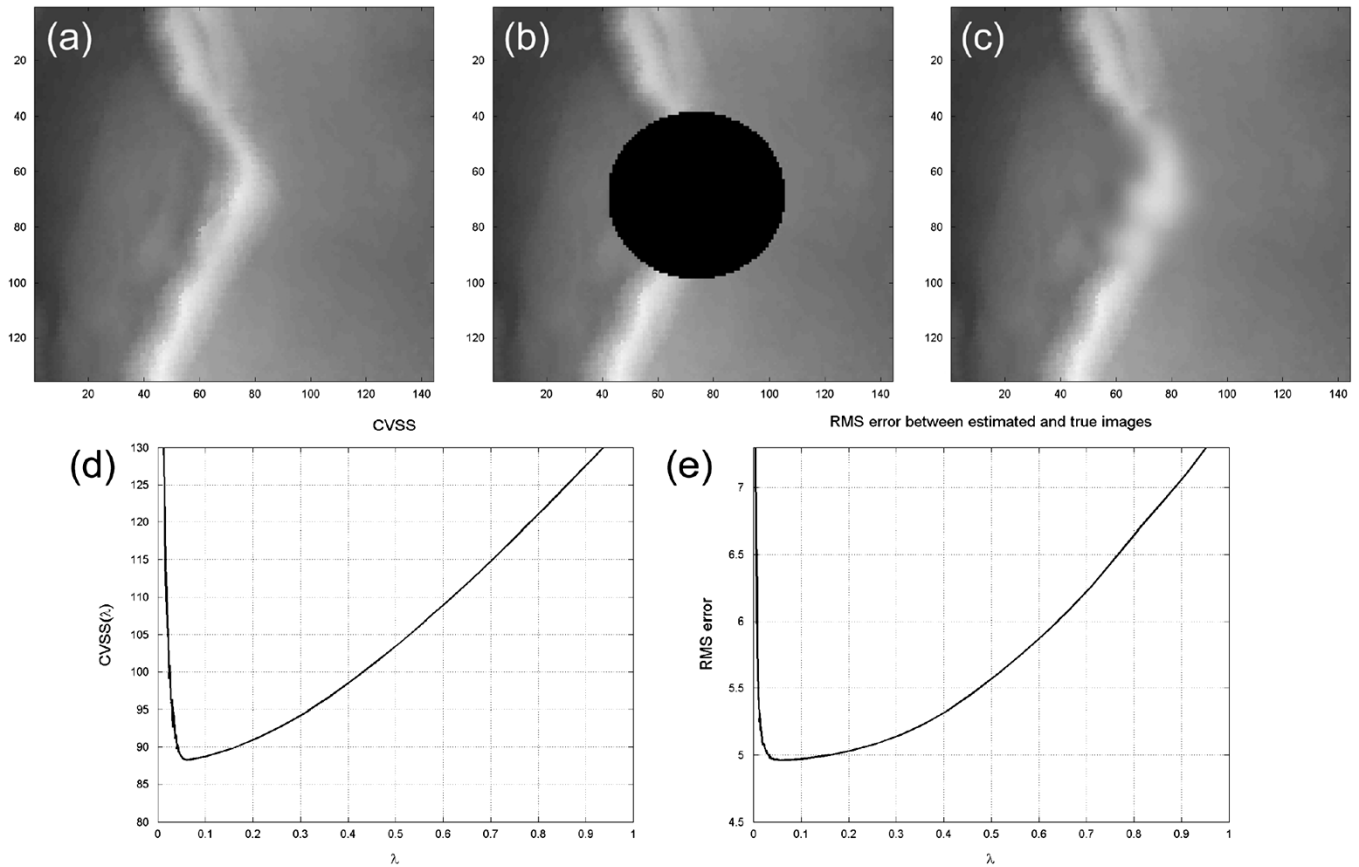
Fig. 9. Quality of the CVSS. (a) aA sample image that does not have a hole. (b) A hole was made. (c) Interpolated image with an optimal weight. (d) CVSS as a function of λ. The CVSS has a minimum when $\lambda = 0.062$. (e) RMS error between true image (a) and the interpolated image (c). The minimum occurs when $\lambda = 0.0652$.

group, it is equivalent to simply filling the regions of missing data with 9×9 identical values that are the same as the corresponding SRTM DEM [Fig. 8(a) and (c)].

The quality of cross-validation in this study is itself validated by simulating the interpolation process with known subimages that do not contain missing data. For example, if a known subimage is selected from Fig. 1 (numbered box 3), we can remove some data and apply our recovery algorithm. The subimage is similar in topographic features to the area shown in Fig. 6. The process is illustrated in Fig. 9. We introduce a hole in Fig. 9(b) and calculate the CVSS [Fig. 9(d)] for each λ ranging from 0 to 2. Then we use the estimated λ, which minimizes the CVSS, for the interpolation process to obtain the image in 9(c). For each value of λ we also calculate the RMS error between the known and the interpolated images. The RMS error is plotted against λ in Fig. 9(e). The CVSS is minimized for $\lambda = 0.062$, while the RMS error has a minimum at $\lambda = 0.065$. This agreement suggests that minimizing the CVSS is a useful method to balance the constraints. Note that the minimum RMS error in Fig. 9(e) is about 5 m. This value is smaller than the relative vertical height accuracy of the SRTM DEM, which is about 10 m.

VI. RESULT AND DISCUSSION

The method presented in the previous section was applied to the entire image of Fig. 1. The registered TOPSAR DEM con-

tains missing data in regions of various sizes. Small subimages were extracted from the DEM. Each subimage is interpolated, and the results are reinserted into the large DEM. The locations and sizes of the subimages are indicated with white boxes in Fig. 10(a). Note the largest region of missing data in the middle of the caldera. This region is not only a simple large gap but also a gap between two swaths. The interpolation is an iterative process and fills up regions of missing data starting from the boundary. If valid data along the boundary (boundaries of a swath for example) contain edge effects, error tends to propagate through the interpolation process. In this case, expanding the region of missing data by a few pixels before interpolation produces better results. If there is a large region of missing data, the spectral content information of valid data can fade out as the interpolation proceeds toward the center of the gap. In this case, sequentially applying the interpolation to parts of the gap is one solution. Due to edge effects along the boundary of the large gap, the interpolation result does not produce topography that matches the surrounding terrain well. Hence, we expand the gap by three pixels to eliminate edge effects. We divided the gap into multiple subimages, and each subimage was interpolated individually.

Finally, we can investigate the effect of the artifact elimination and the interpolation on simulated interferograms. It is often easier to see differences in elevation in simulated interferograms than in conventional contour plots. In addition, simulated interferograms provide a measure of how sensitive the interfero-
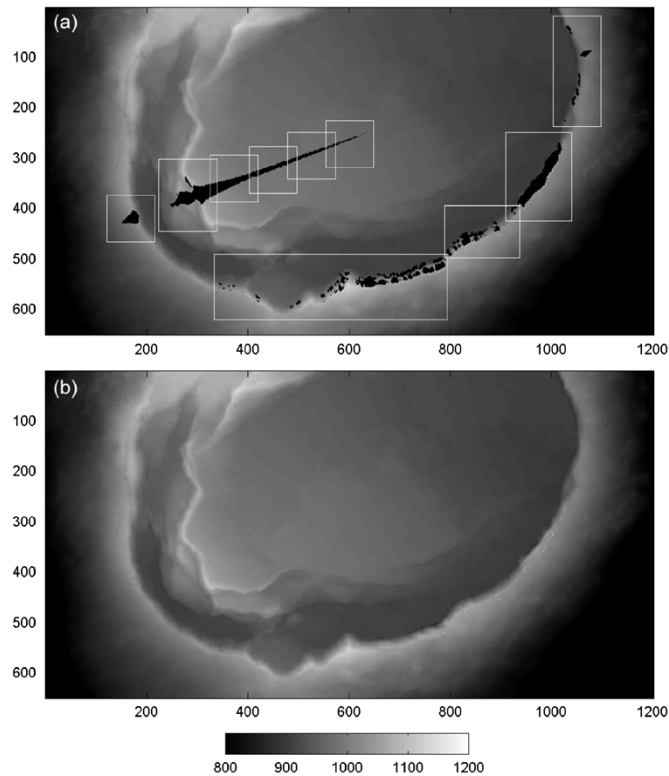
Fig. 10. (a) Original TOPSAR DEM and (b) the reconstructed DEM after interpolation with PE filter and SRTM DEM constraints. The grayscale is altitude in meters, and the spatial extent is about 12 km across the image.

gram is to the topography. Fig. 11 shows georeferenced simulated interferograms from three DEMs; the registered TOPSAR DEM, the TOPSAR DEM after the artifact elimination, and the TOPSAR DEM after the interpolation. In all interferograms, a C-band wavelength is used, and we assume a 452-m perpendicular baseline between two satellite positions. This perpendicular baseline is realistic [2]. The fringe lines in the interferograms are approximately height contour lines. The interval of the fringe lines is inversely proportional to the perpendicular baseline [10], and in this case one color cycle of the fringes represents about 20 m. Note in Fig. 11(a) that the fringe lines are discontinuous across the long region of missing data inside the caldera. This is due to artifacts in the original TOPSAR DEM. After eliminating these artifacts the discontinuity disappears [Fig. 11(b)]. Finally the missing data regions are interpolated in a seamless manner [Fig. 11(c)].

VII. CONCLUSION

The aircraft roll artifacts in the TOPSAR DEM were eliminated by subtracting the difference between the TOPSAR and SRTM DEMs. A 2-D PE filter derived from the existing data and the SRTM DEM for the same region are then used as interpolation constraints. Solving the inverse problem constrained with both the PE filter and the SRTM DEM produces a high-quality interpolated map of elevation. Cross-validation works well to select optimal constraint weighting in the inversion. This objective criterion results in less biased interpolation and guarantees the best fit to the SRTM DEM. The quality of many other TOPSAR DEMs can be improved similarly.
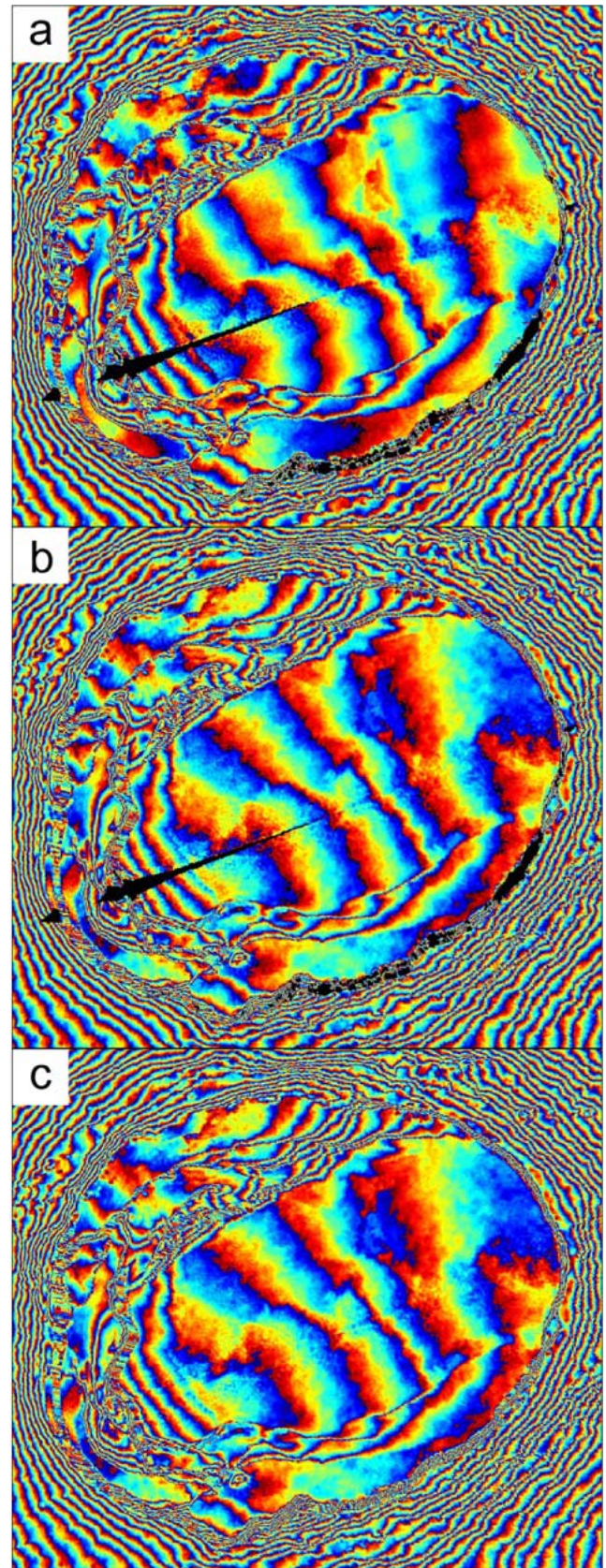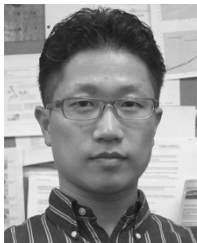

Fig. 11. Simulated interferograms from (a) the original registered TOPSAR DEM, (b) the DEM after the artifact was removed, and (c) the DEM interpolated with PE filter and the SRTM DEM. All the interferograms were simulated with the C-band wavelength (5.6 cm) and a perpendicular baseline of 452 m. Thus, one color cycle represents 20-m height difference.
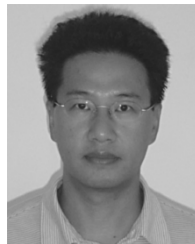
REFERENCES

[1] H. A. Zebker and R. M. Goldstein, "Topographic mapping from interferometric synthetic aperture radar observations," *J. Geophys. Res.*, vol. 91, no. B5, pp. 4993–4999, 1986.

[2] F. Amelung, S. Jónsson, H. Zebker, and P. Segall, "Widespread uplift and 'trapdoor' faulting on Galápagos volcanoes observed with radar interferometry," *Nature*, vol. 407, no. 6807, pp. 993–996, 2000.

[3] S.-H. Yun, P. Segall, and H. Zebker, "Constraints on magma chamber geometry at Sierra Negra volcano, Galápagos Islands, based on InSAR observations," *J. Volcanol. Geothermal Res.*, 2005, to be published.

[4] H. A. Zebker, S. N. Madsen, J. Martin, K. B. Wheeler, T. Miller, Y. L. Lou, G. Alberti, S. Vetrella, and A. Cucci, "The TOPSAR interferometric radar topographic mapping instrument," *IEEE Trans. Geosci. Remote Sens.*, vol. 30, no. 5, pp. 933–940, Sep. 1992.

[5] S. N. Madsen, H. A. Zebker, and J. Martin, "Topographic mapping using radar interferometry: Processing techniques," *IEEE Trans. Geosci. Remote Sens.*, vol. 31, no. 1, pp. 246–256, Jan. 1993.

[6] Y. Kobayashi, K. Sarabandi, L. Pierce, and M. C. Dobson, "An evaluation of the JPL TOPSAR for extracting tree heights," *IEEE Trans. Geosci. Remote Sens.*, vol. 38, no. 6, pp. 2446–2454, Nov. 2000.

[7] J. F. Claerbout, *Earth Sounding Analysis: Processing Versus Inversion*. Oxford, U.K.: Blackwell, 1992. See also http://sepwww.stanford.edu/sep/prof/index.html.

[8] J. F. Claerbout and S. Fomel. (2002) Image estimation by example: Geophysical soundings image construction (Class Notes). [Online]. Available: http://sepwww.stanford.edu/sep/prof/index.html.

[9] G. Wahba, *Spline Models for Observational Data*, ser. Applied Mathematics. Philadelphia, PA: SIAM, 1990.

[10] H. A. Zebker, P. A. Rosen, and S. Hensley, "Atmospheric effects in interferometric synthetic aperture radar surface deformation and topographic maps," *J. Geophys. Res.*, vol. 102, no. B4, pp. 7547–7563, 1997.

Jun Ji received the B.S. and M.S. degrees in petroleum engineering from Seoul National University, Seoul, Korea, in 1987 and 1989, respectively, and the Ph.D. in geophysics from Stanford University, Stanford, CA, in 1995.

He was a Research Geophysicist with 3DGeo Development Inc., Mountain View, CA, in 1996. Since 1997, he has been a faculty member in the Department of Information System Engineering, Hansung University, Seoul.

Howard A. Zebker (M'87–SM'89–F'99) received the B.S. degree from the California Institute of Technology, Pasadena, the M.S. degree from the University of California, Los Angeles, and the Ph.D. degree from Stanford University, Stanford, CA, in 1976, 1979, and 1984, respectively.

He holds a joint appointment in the Geophysics and Electrical Engineering Departments at Stanford and studies Earth processes from the viewpoint of spaceborne instruments. His group is involved in basic research ranging from crustal deformation related to earthquakes and volcanoes to global environmental problems as evidenced in the flow-and distribution of ice in the polar regions. The group is also developing new observational technologies such as radar interferometry. He is involved in the definition and scientific applications of new spaceborne imaging systems, especially those containing imaging radar systems.

Sang-Ho Yun (S'00) received the M.S. degree in geophysics and the M.S. degree in electrical engineering from Stanford University, Stanford, CA, in 2003 and 2005, respectively. He is currently pursuing the Ph.D. degree in geophysics at Stanford University, working on volcanic deformation source modeling based on satellite radar interferometry observations of the volcanoes in Galápagos Islands.

His current research interests include radar interferometry, crustal deformation, image processing, and data fusion.

Paul Segall received the Ph.D. degree in geology from Stanford University, Stanford, CA, in 1981.

From 1981 to 1993, he was with the U.S. Geological Survey as a Research Geologist and a Project Chief. Since 1987, he has been a faculty member in the Geophysics Department, Stanford University, where he is leading the Crustal Deformation and Fault Mechanics Group.

Dr. Segall received the U.S. Geological Survey Special Achievement Award in 1984 and the James B. Macelwane Medal from the American Geophysical Union (AGU) in 1990. He was awarded the Citation for Excellence in Refereeing from AGU in 2002. He is currently a Fellow of the AGU and the Geological Society of America.